Proceedings of the
Annual Stability Conference
Structural Stability Research Council
Louisville, Kentucky, April 13-16, 2021

On the lateral-torsional buckling behavior of channel beams

Rodrigo Gonçalves[1]

Abstract
This paper presents the results of a parametric study concerning the elastic buckling behavior and strength (elastoplastic buckling, including geometric imperfections and residual stresses) of steel channels subjected to major-axis bending and undergoing lateral-torsional buckling. The results are obtained using a two-node geometrically exact beam finite element developed by the author, which can handle large displacements, finite rotations, torsion-related warping, Wagner effects, plasticity, residual stresses and geometric imperfections. It is shown that the lateral-torsional post-buckling behavior of channel beams is asymmetric, which means that the direction of the geometric imperfection influences their strength (sometimes considerably). Furthermore, it is demonstrated that the cross-section geometry, loading and support conditions influence the strength significantly and lead to a scatter of results which hinder the definition of a single buckling curve for design purposes. Despite this scatter, in all cases considered, the buckling strengths fall significantly above those predicted by the current version of Eurocode 3.

1. Introduction

Although channel sections are widely used in the construction industry, their analysis and design constitute a rather challenging problem, since the cross-section shear center and centroid do not coincide and the shear center does not lie in the cross-section (hence self-weight causes first-order torsion). In the particular case of the safety checking of hot-rolled channel section beams against lateral-torsional (LT) buckling, the current version of Eurocode 3 (CEN 2005) prescribes the use of the lowest buckling curve, which "knocks down" severely their plastic moment resistance. Despite this situation, recent research concerning hot-rolled channels is quite scarce, a situation which is in sharp contrast with the case of cold-formed steel lipped channels, which have deserved a significant amount of attention due to their susceptibility to local and distortional buckling (e.g. Kwon & Hancock 1993, Martins et al. 2018, Ye et al. 2019). A few years ago, a German research project investigated the effect of biaxial bending and torsion, using numerical and experimental tests, and proposed design formulas for hot-rolled I-sections and channels (Kindman & Frickel 2002, Frickel 2002, Kindmann & Wolf 2004, Lindner & Glitsch 2004). More recently, Snijder et al. (2008) performed a numerical parametric study concerning hot-rolled channels subjected to web loads (hence subjected to first-order torsion) and proposed a design equation which was shown to be more accurate than that by Lindner & Glitsch (2004).

[1] Associate Professor, CERIS and Universidade Nova de Lisboa, Portugal, <rodrigo.goncalves@fct.unl.pt>

This paper extends previous research, concerning the LT buckling behavior of I-section beams under uniaxial and biaxial bending (Gonçalves & Camotim 2017, Gonçalves 2019, 2020), to hot-rolled (compact) channel section beams loaded through their shear center, and provides a new insight on their elastic and elastoplastic (including imperfections) post-buckling behavior. For this goal, a numerical parametric study is carried out using a beam finite element developed by the author (Gonçalves 2016), which is geometrically exact and accounts for torsion-related warping, Wagner effects (Wagner, 1929), plasticity, residual stresses and geometric imperfections. At this point it is worth noting that the so-called "geometrically exact beam theory" originated from the works of Reissner (1972, 1973) and Simo (1985), being characterized by a key feature: no geometric simplifications are introduced besides the assumed kinematics. In particular, each beam cross-section is mapped using a translation and a genuine finite rotation, using a rotation tensor. In the present beam finite element, torsion-related warping is further included in the kinematic description (as in, e.g., Simo & Vu-Quoc 1991, Gruttmann et al. 2000), since this is essential to capture the torsional behavior of thin-walled members.

2. The geometrically exact thin-walled beam finite element

The thin-walled beam finite element employed in this work is described in detail in Gonçalves (2016, 2019) and therefore only a brief account of its main features is discussed in this paper. In addition, validation examples concerning channel section members are provided. The element has two nodes and interpolates seven independent kinematic parameters using Lagrange linear functions (14 DOF element). These parameters correspond to the translation of the cross-section center C (components $\hat{u}_1, \hat{u}_2, \hat{u}_3$), the rotation vector about C (components $\theta_1, \theta_2, \theta_3$) and the weight of the warping function (p) . The initial configuration is assumed unsheared and untwisted, being solely defined by the position of the end nodes and the orientation of one of the cross-section axes (which is assumed constant throughout the beam length). The warping function is subdivided into a cross-section mid-line component, obtained using the classic theory of thin-walled bars (e.g., Vlasov, 1958) and a through-thickness component calculated using Kirchhoff's thin plate assumption.

The equilibrium equations are obtained using the virtual work principle, written in terms of Green-Lagrange strains and second Piola-Kirchhoff stresses, which together with a St. Vénant-Kirchhoff material law ensures capturing Wagner effects (Wagner, 1929). Small strain plasticity is implemented, using the von Mises yield function and an associated flow rule, without hardening. The material parameters are thus Young's modulus E, Poisson's ratio ν and the uniaxial yield stress f_y. The residual stresses are first converted into residual strains, which are added to the compatible strains.

Numeric integration is carried out using Gauss quadrature. For an elastic material behavior, cross-section integration is exact by using, in each wall, 3 points along the mid-line direction and 2 points along the thickness. A single point is considered along the length, to avoid locking problems. For the elastoplastic case, a higher number of Gauss points is required, as explained next. The equilibrium paths are obtained using a standard incremental-iterative scheme with load-displacement control. The procedure was implemented in MATLAB (2010).

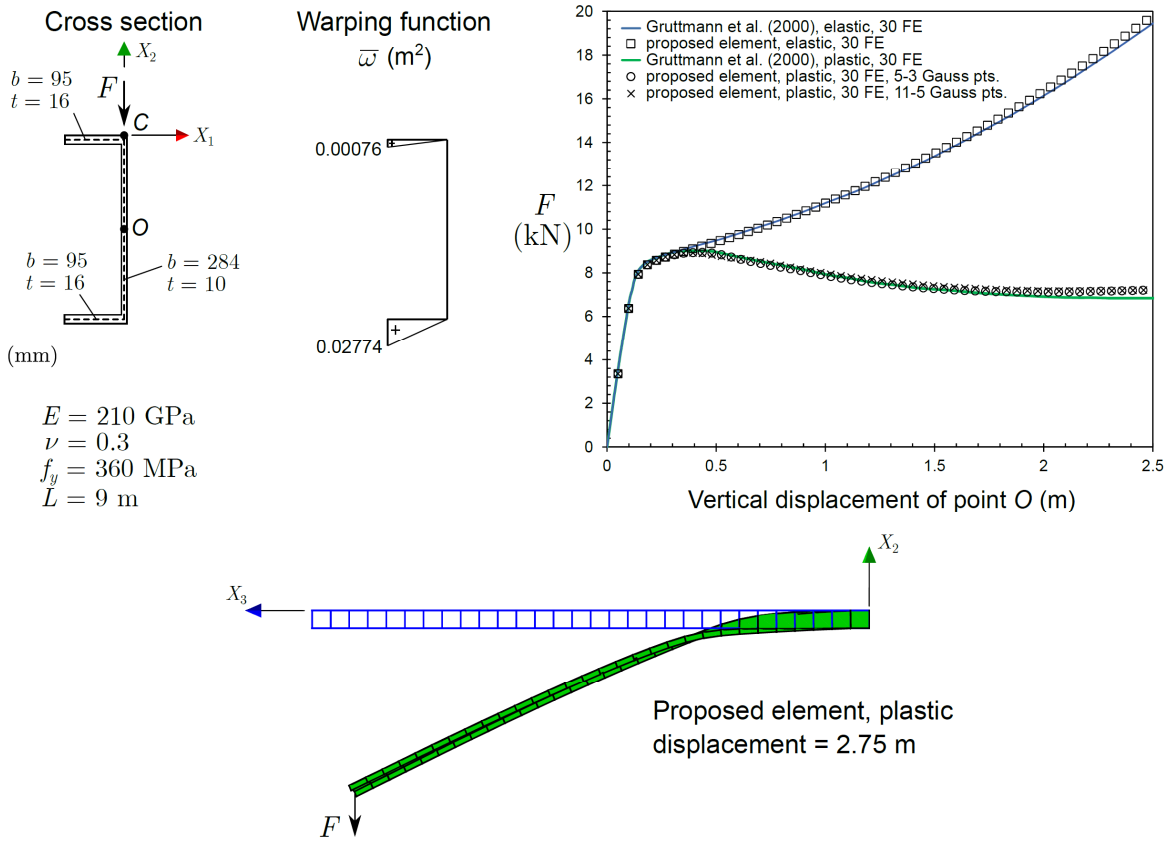

Figure 1: Validation example: elastic and plastic lateral-torsional buckling of a channel cantilever beam

Several validation examples of the proposed beam finite element are provided in Gonçalves (2019) and include residual stresses, geometric imperfections and plasticity. However, only a single example concerns channels. For this reason, this example is repeated here, for completeness of the paper, and an additional example is provided that demonstrates the accuracy of the element for curved members undergoing complex torsion-bending and large displacements. In both cases the forces are applied at a cross-section point, since a shear center load cannot be consistently applied in a shell element model undergoing large displacements.

First, the cantilever channel beam proposed by Gruttmann et al. (2000) is examined. The problem geometry, material parameters and loading are shown in Fig. 1, together with the mid-line warping function adopted, which corresponds to a rotation about the point of load application (point C), and the results obtained. The graph compares the elastic and elastoplastic load-displacement curves for point O, obtained with the proposed element and a similar two-node element (Gruttmann et al. 2000) that interpolates the cross-section basis vectors of the end nodes (instead of the rotation vector) and discretizes the cross-section into 44 rectangles. All results were obtained using 30 equal length finite elements.

The load-displacement curves in the graph for the elastic case virtually match, with a maximum difference which is below 2% and occurs for the maximum vertical displacement considered. For

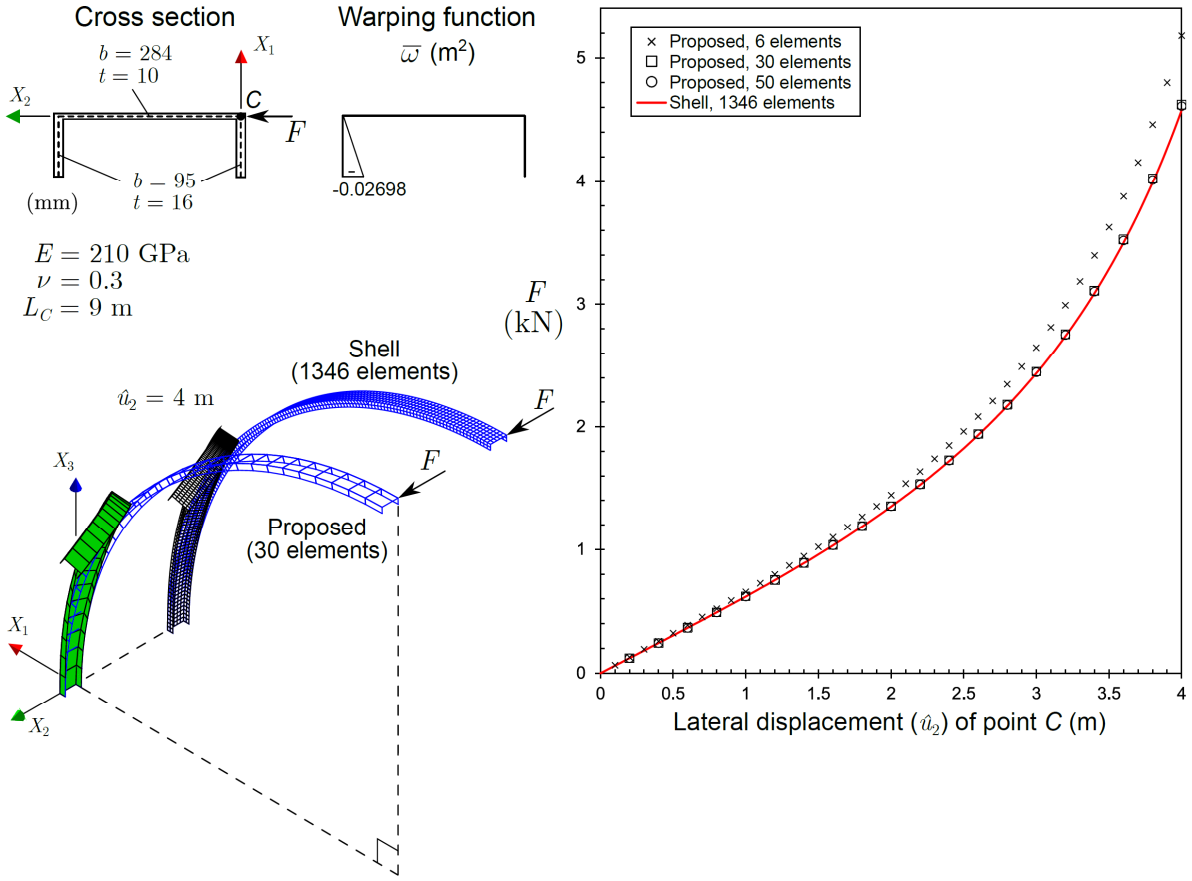

Figure 2: Validation example: 90º circular elastic cantilever loaded by an out-of-plane force

the elastoplastic case, using the proposed element with 5-3 Gauss points (along the mid-line and through-thickness directions, respectively) already matches the solution of Gruttmann et al. (2000), with the maximum load falling within 1% of the latter.

The second example is shown in Fig. 2. The cross-section geometry and material parameters are kept, but the cantilever is initially bent in a 90º circular arc with a total length of 9 meters, measured along the line corresponding to point C. The load is applied at the flange-web mid-line intersection and therefore the mid-line warping function is slightly different than that shown in Fig. 1. This example aims at validating the proposed element for curved members undergoing complex flexural-torsional phenomena involving large displacements. Only elastic behavior is considered.

The graph in Fig. 2 plots the load-displacement curves obtained with the proposed finite element, for three discretization levels, and a refined MITC-4 (Mixed Interpolation of Tensorial Components) shell finite element model, analyzed using ADINA (Bathe, 2019). The proposed element does not lead to accurate solutions when only 6 elements are employed, but the maximum difference with respect to the shell model decreases to 1.0% with 30 elements and 0.7% with 50 elements. The deformed configurations in the figure concern a lateral displacement of the free end ($\hat{u}_2$) equal to 4 meters and clearly demonstrate an excellent match.

3. Elastic post-buckling and strength of channel section beams

3.1 Introduction

The next Sections assess the LT post-buckling elastic behavior (Section 3.2) and strength (Section 3.3) of channels, using the proposed beam finite element. This Section reviews some fundamental concepts and explains details of the parametric study carried out.

According to clause 6.3.2.1 of Eurocode 3 (CEN, 2005), a laterally unrestrained member under major axis bending is checked against LT buckling with

$$\frac{M_{Ed}}{\chi_{LT} M_{Rk}/\gamma_{M1}} \leq 1.0, \tag{1}$$

where M_{Ed} is the design value of the maximum moment acting on the beam, M_{Rk} is the cross-section characteristic moment resistance, γ_{M1} is the partial factor for resistance of members to instability assessed by member checks (the recommended value is 1.0) and χ_{LT} is the reduction factor for LT buckling, pertaining to the relevant buckling curve and the LT slenderness

$$\bar{\lambda}_{LT} = \sqrt{\frac{M_{Rk}}{M_{cr}}}, \tag{2}$$

where M_{cr} is the LT critical buckling moment, obtained from a standard linear stability analysis. Two methods are provided for obtaining the reduction factor χ_{LT}, namely (i) the "general case" (GC) of clause 6.3.2.2 and (ii) the "special case" (SC) of clause 6.3.2.3, which applies to rolled I-sections or equivalent welded sections. Therefore, for channels, only the GC can be used, and buckling curve *d* (the most detrimental) is prescribed. The reduction factor is thus obtained from

$$\chi_{LT} = \frac{1}{\Phi_{LT} + \sqrt{\Phi_{LT}^2 - \bar{\lambda}_{LT}^2}} \leq 1.0, \tag{3}$$

$$\Phi_{LT} = \frac{1}{2}\left(1 + \alpha_{LT}\left(\bar{\lambda}_{LT} - 0.2\right) + \bar{\lambda}_{LT}^2\right), \tag{4}$$

with $\alpha_{LT} = 0.76$ for curve *d*, although no reduction needs to be considered if $\bar{\lambda}_{LT} \leq \bar{\lambda}_{LT,0}$, where $\bar{\lambda}_{LT,0}$ is provided in the National Annexes and the recommended value for rolled or equivalent welded sections is 0.4.

For comparison, it is also worth recalling the proposal by Snijder et al. (2008), even though it was developed for channels subjected to web loads (hence subjected to first-order torsion). This proposal relies on a modified slenderness concept and reads

$$\bar{\lambda}_T = \begin{cases} 1 - \bar{\lambda}_{LT} & \text{if } 0.5 \leq \bar{\lambda}_{LT} < 0.8 \\ 0.43 - 0.29\bar{\lambda}_{LT} & \text{if } 0.8 \leq \bar{\lambda}_{LT} < 1.5 \\ 0 & \text{if } 1.5 \leq \bar{\lambda}_{LT} \end{cases} \tag{5}$$

$$\bar{\lambda}_{MT} = \bar{\lambda}_{LT} + \bar{\lambda}_T \tag{6}$$

$$\Phi_{LT} = \frac{1}{2}\left(1 + 0.21\left(\bar{\lambda}_{MT} - 0.2\right) + \bar{\lambda}_{MT}^2\right), \tag{7}$$

$$\chi_{LT} = \frac{1}{\Phi_{LT} + \sqrt{\Phi_{LT}^2 - \bar{\lambda}_{MT}^2}} \leq 1.0. \tag{8}$$

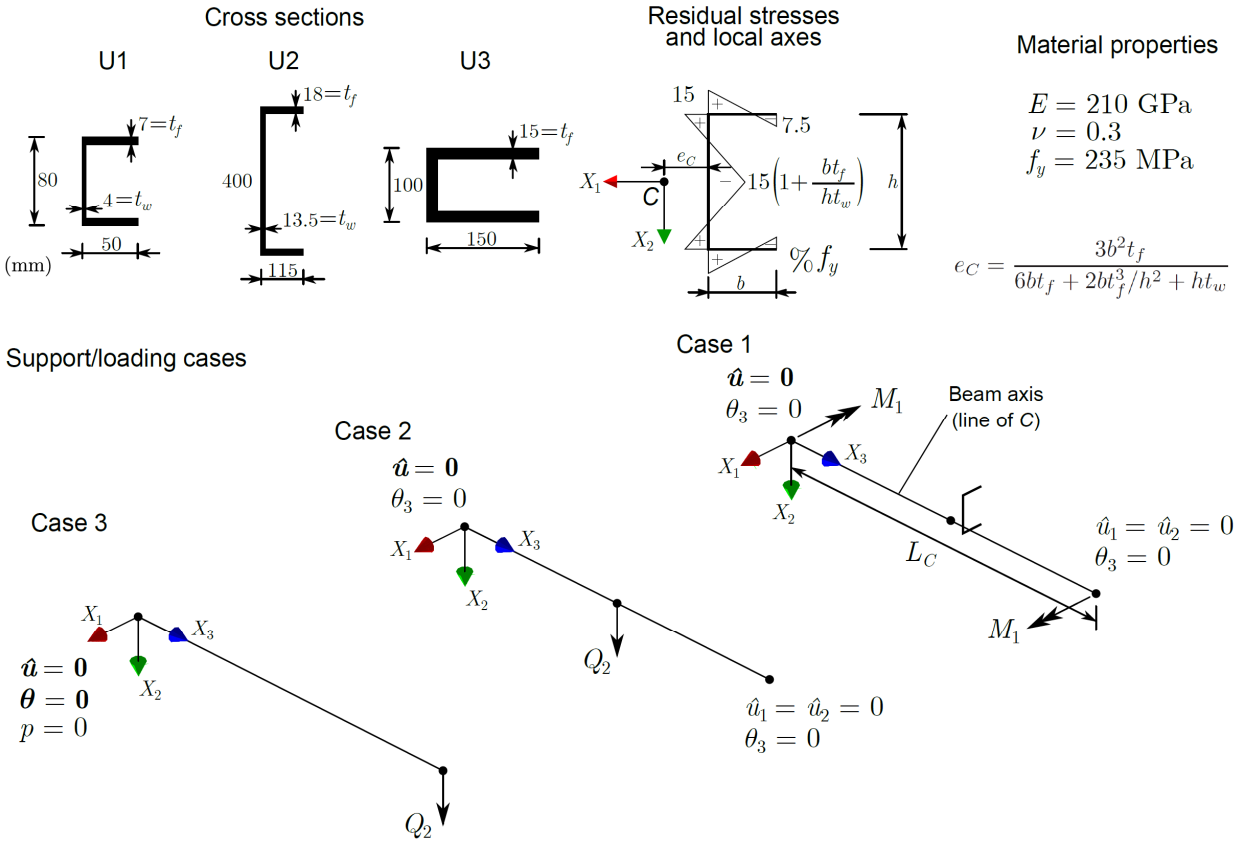

Figure 3: Cross-sections geometries, residual stresses, material properties and support/load cases considered

The cases analyzed in the next Sections are displayed in Fig 3. The dimensions of sections U1 and U2 essentially correspond to those of standard UPEs 80 and 400, whereas section U3 was selected because the major axis is vertical rather than horizontal. All cross-sections are "class 1" (compact) according to Eurocode 3, meaning that they can develop a plastic hinge with the rotation capacity required for a plastic analysis (local buckling does not affect their strength). The residual stresses are similar to those reported by Lindner & Glitsch (2004) for an UPE 200, but the value at the web mid-height is changed an written as a function of the geometric parameters, to obtain null stress resultants (a mid-line approximation was used to obtain the formula shown in the figure).

The cross-section center C coincides with the shear center and the loads are applied at this point, which prevents first-order torsion for straight members. Three support/load cases are considered, with the beam axis always coinciding with the line defined by point C and having length L_C. Cases 1 and 2 correspond to standard "fork" supports and Case 3 corresponds to cantilevers. In all cases a lateral geometric imperfection is considered, with maximum amplitude equal to $e_0 = L_C/1000$,

as in similar investigations (Gonçalves 2019, Taras & Greiner 2010), either positive or negative along X_1. For cases 1 and 2 the imperfection is shape is given by $\pm e_0 \sin(\pi X_3/L_C)$, whereas for case 3 it reads $\pm e_0 (X_3/L_C)^2$.

Four types of analyses are carried out:

(i) Linear Stability Analyses (LSAs), to calculate critical bifurcation loads without the effect of pre-buckling deflections and imperfections. The beams are assumed straight. These analyses are carried out using the geometrically exact Vlasov beam formulation proposed by Gonçalves (2012), since it is very efficient for this purpose.

(ii) Non-linear stability analyses (NSAs). In this case the bifurcation loads are obtained by tracing the true (non-linear) equilibrium path of the straight and elastic member, pinpointing the first occurrence of a negative eigenvalue in the tangent stiffness matrix (excluding limit points). These bifurcation loads naturally take into account pre-buckling deflections.

(iii) Geometric non-linear analyses with imperfections (GNIAs). The non-linear equilibrium path is calculated assuming an elastic material, including geometric imperfections.

(iv) Geometric and material non-linear analyses with imperfections (GMNIAs). These analyses are assumed to retrieve the "true" collapse loads, since all non-linearities are included, as well as residual stresses and geometric imperfections.

In all cases 30 equal length finite elements are used and, for the elastoplastic cases, 3-11 Gauss points are considered along the thickness/mid-line of each wall, as in previous work (Gonçalves, 2019). Even though the load-displacement paths are calculated up to large displacements, it should be noted that in some cases these paths are not realistic, as large strains occur and local buckling may influence the results. Nevertheless, the shape of the path is essential to help grasping the behavior of the members under consideration.

It is also useful to recall that, for elastic and simply supported I-beams subjected to uniform bending, the NSA critical moment can be estimated through (Pi & Trahair 1992)

$$M_{cr}^{NSA} = \beta M_{cr}^{LSA}, \tag{9}$$

$$\beta = \frac{1}{\sqrt{\left(1-\frac{I_z}{I_y}\right)\left(1-\left(GJ+\frac{\pi^2 E I_\omega}{L^2}\right)/2EI_y\right)}} \approx \frac{1}{\sqrt{\left(1-\frac{I_z}{I_y}\right)}}, \tag{10}$$

where I_z and I_y are the second moments of area about the weak and strong central principal axes, respectively, J is the St. Venant torsion constant, I_ω is the warping constant, G is the shear modulus and L is the beam length. Although these formulas do not apply to channels, they provide some insight concerning the beam behavior. In particular, using the simplified formula one obtains $\beta_{U1} = 1.15$, $\beta_{U2} = 1.03$ and $\beta_{U3} = 1.83$, which makes it possible to anticipate that, for section U3, the NSA critical load will be substantially higher than the LSA one.

3.2 Elastic post-buckling behavior

The elastic post-buckling behavior is assessed first, using GNIAs. Fig. 4 shows the load-displacement paths obtained for each support/load case and sections U1 and U2. For section U1, $L_C = 4$ m is adopted, whereas for section U2 one uses $L_C = 5$ m, leading to $0.82 \leq \bar{\lambda}_{LT} \leq 1.10$.

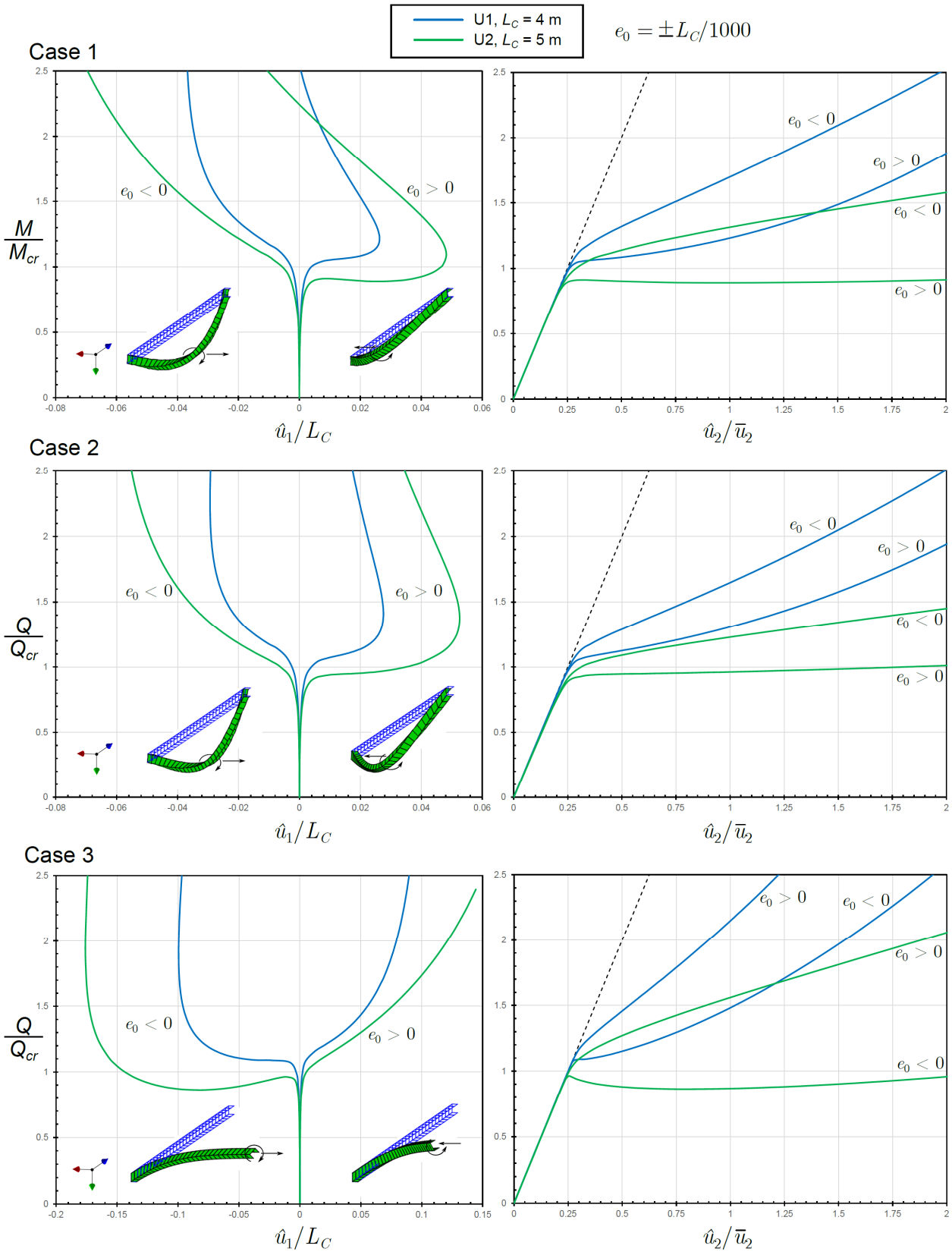

Figure 4: Normalized elastic post-buckling load-displacement paths

The vertical axes are normalized with respect to M_{cr}^{LSA} and the horizontal axes are normalized with respect to L_C (left graphs) and $\bar{u}_2$ (right graphs), where $\bar{u}_2$ is a factor that makes the vertical displacement in a linear analysis equal to 1 when the load equals a scaling factor α times the critical load — in the figure $\alpha = 4$ is adopted (a higher/lower value simply leads to an increase/decrease of all slopes) and one has $\bar{u}_2 = \alpha L^2 M_{cr}/8EI_y$ for Case 1, $\bar{u}_2 = \alpha L^3 Q_{cr}/48EI_y$ for Case 2 and $\bar{u}_2 = \alpha L^3 Q_{cr}/3EI_y$ for Case 3. The graphs also show typical deformed configurations for the U1 section beams, with the arrows indicating the directions of the lateral displacement and the twist.

The results in Fig. 4 prompt the following remarks:

(i) The left-side graphs show that the post-buckling paths are not symmetric and, while most of them are stable (some highly stable), those concerning the U2 section and Cases 1 and 3 exhibit negative stiffness near the bifurcation load — features which are not observed for I-section beams (Gonçalves 2019). This enables anticipating that the buckling strength will be sensitive to the imperfection magnitude and direction (positive or negative). Note also that the direction of the imperfection associated with the most flexible path depends on the support/load case considered: it is positive for Cases 1 and 2, but negative for Case 3.

(ii) The right-side graphs indicate that, in general, the paths for section U2 fall below those of section U1, hinting that the buckling resistance of U2 section members will be generally lower, irrespective of the imperfection direction (this issue will be further examined in Section 3.3).

(iii) The right-side graphs also show that, for each case, the two paths for section U2 break out for loads below the bifurcation load, whereas for section U1 this occurs for somewhat higher loads. This agrees with the β values for each section ($\beta_{U1} = 1.15$, $\beta_{U2} = 1.03$).

In conclusion, the results in Fig. 4 demonstrate that the shape of the elastic post-buckling equilibrium path is strongly influenced by the direction of the imperfection, the support/load conditions and the cross-section geometry. However, conclusions concerning the buckling *strength* of these members can only be drawn by performing GMNIAs (Section 3.3). Nevertheless, since the behavior for Cases 1 and 2 is somewhat similar (the load and support conditions are similar), only the latter will be considered in the GMNIA calculations.

Before ending this Section, U3 cantilever beams (Case 3) with $L_C = 8$ m are analyzed, since this case already illustrates the fundamental aspects of the post-buckling behavior of beams with this cross-section. The major axis is parallel to X_2 and therefore the tip load is applied along X_1 (instead of X_2, as in Case 3). Consequently, the imperfection is provided along X_2 and its sign is irrelevant, since the cross-section is symmetric about X_1. On the other hand, the load direction is not irrelevant and thus positive and negative the tip forces Q_1 are considered.

The graph in Fig 5 plots the load-displacement curves for the lateral $\hat{u}_2$ and vertical $\hat{u}_1$ displacements, for positive and negative Q_1, as well as the LSA and NSA bifurcation points. The figure also shows the successive deformed configurations of the two beams. These results prompt the following remarks:

(i) The LSA bifurcation loads are quite different for positive or negative Q_1, which agrees with the well-known buckling behavior of mono-symmetric sections bent in a plane of symmetry

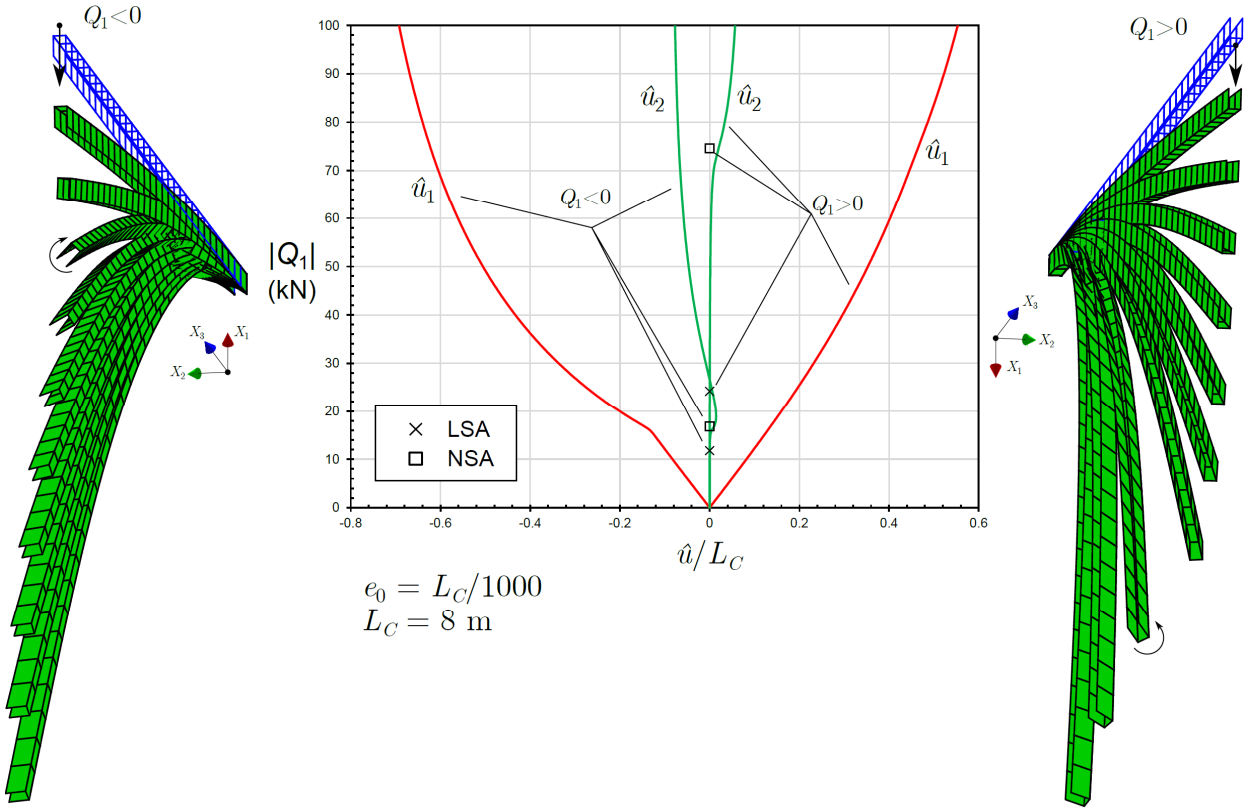

Figure 5: Elastic post-buckling paths and deformed configurations for an 8-meter length cantilever with section U3 and subjected to a positive/negative tip load along X_1

(see, e.g., Trahair, 1993) — tensile/compressive stresses due to bending reduce/increase twisting and this effect increases with the distance of the stresses with respect to the shear center, hence $Q_1 < 0$ leads to lower bifurcation loads.

(ii) The difference between the LSA and NSA bifurcation loads is quite large for negative Q_1, but it is remarkably larger for positive Q_1. In particular, $M_{cr}^{NSA}/M_{cr}^{LSA} = 3.08$ for positive Q_1 and $M_{cr}^{NSA}/M_{cr}^{LSA} = 1.43$ for negative Q_1. This is due to the combination of the effect mentioned in the previous item with the fact that the I_z/I_y ratio is quite high for this section ($\beta_{U3} = 1.83$). Similar conclusions have been obtained by the author (Gonçalves 2019) for a doubly symmetric wide flange I-section. However, for section U3, the β parameter does not lead to accurate $M_{cr}^{NSA}/M_{cr}^{LSA}$ estimates, since Eq. (10) was not developed for mono-symmetric sections.

(iii) The deformed configurations show that the twist of the free end section occurs for very different vertical displacement (hence load) values. However, even for negative Q_1 (which leads to the lowest bifurcation load), the twist occurs for quite large displacements, which means that these beams will be essentially governed by the serviceability limit state, rather than the ultimate limit state.

3.3 Buckling strength

In the previous Section it was shown that the elastic post-buckling behavior of channel beams is quite peculiar, exhibiting non-symmetric paths with unstable branches. This section focuses on the elastoplastic buckling strength, including imperfections and residual stresses.

The elastoplastic behavior of channel beams can differ significantly from its elastic counterpart, since the location of the shear center moves as plasticity spreads. Handelman (1951) and Johnson & Mellor (1957) discussed the geometrically linear case for some material laws and cross-section geometries, including channels with constant thickness. For an elastic-perfectly plastic material, if the channel flanges become fully plastic due to bending, the shear force is carried by the web and thus the shear center moves to the center of the web. This eccentricity is not particularly relevant for slender beams, which start to buckle (LT buckling in the present case) before the flanges become fully plastic, but may be important otherwise, as mentioned further ahead.

The strength of channel section beams is assessed by performing GMNIAs, considering either positive or negative imperfections e_0. As already mentioned, the support/load Case 1 is not analyzed, as it is quite similar to Case 2. Moreover, Section U3 is not considered, as it will be mostly governed by the serviceability limit state. The beam lengths considered vary between 1.3 and 7 m, for section U1, and 4 to 10 m, for section U2. The results are shown in Figs. 6 (section U1) and 7 (section U2). In each figure, the graphs (a) show the GMNIA reduction factors χ_{LT} (maximum GMINIA load divided by the plastic capacity), as a function of the slenderness $\bar{\lambda}_{LT}$, as well as the Eurocode 3 buckling curves and Eq. (8), by Snijder et al. (2008), whereas graphs (b)-(c) plot the normalized load-displacement curves for each case. It is recalled that, for channel section beams, Eurocode 3 prescribes the lowest red curve in graphs (a) (curve *d*).

Concerning the results for section U1 (Fig. 6), attention is called to the following aspects:

(i) For Case 2, graph (a) shows that the buckling strengths are significantly lower for a positive imperfection. This is in agreement with the elastic post-buckling paths obtained for this case (the middle graphs in Fig. 4), which exhibit a lower stiffness near the bifurcation load for $e_0 > 0$, and is further confirmed by observing the maxima of the load-displacement paths in graph (b) of Fig. 7.

(ii) For Case 3, examining graphs (a) and (c) makes it possible to conclude that, even though the buckling strengths for either positive or negative imperfection do not differ as dramatically as in Case 2, the load-displacement paths are again asymmetric and agree with the elastic post-buckling paths (bottom graphs in Fig. 4). The only exception occurs for the lowest slenderness (0.930), where the buckling strengths are virtually equal, even though the paths are not symmetric.

(iii) In terms of buckling curves (graph (a)), it is concluded that the GMNIA results fall well above all the Eurocode 3 curves and, naturally, also the curved proposed by Snijder et al. (2008), as it was developed for eccentric loading. Remarkably, the reduction factors for Case 3 fall above the "perfect column" curve (given by $\chi_{LT} = 1$ for $\bar{\lambda}_{LT} < 1$, and $\chi_{LT} = 1/\bar{\lambda}_{LT}^2$ for $\bar{\lambda}_{LT} \geq 1$) — similar results for I-section members have been obtained by Taras & Greiner (2010) and Gonçalves (2019).

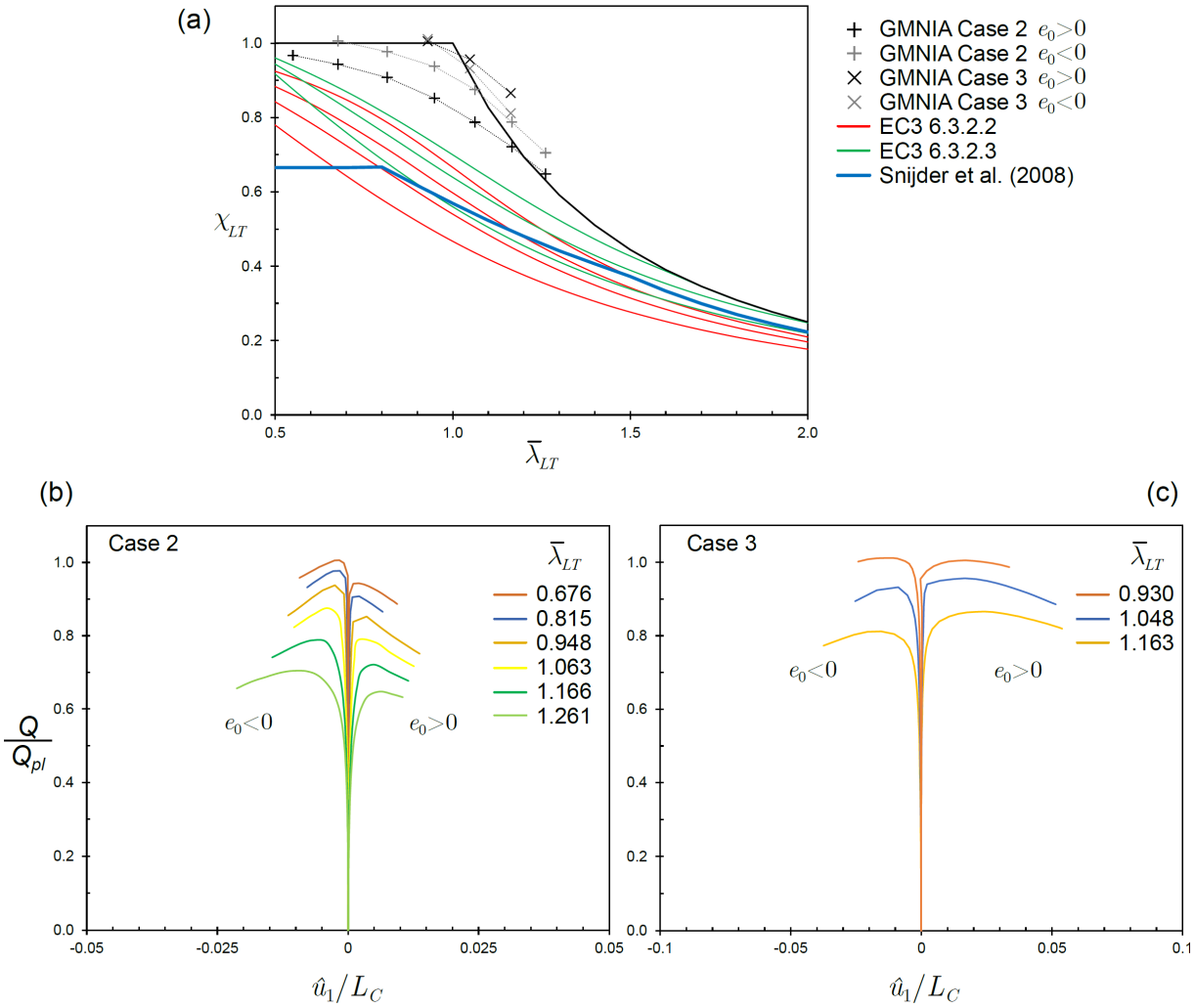

Figure 6: GMNIA results for cross-section U1 and Cases 2-3: (a) reduction factors and (b)-(c) normalized load-displacement paths

Concerning the results for section U2, reported in Fig. 7:

(i) For Case 2, as in the case of section U1, graph (a) shows that the buckling strengths are much lower for positive imperfections, confirming once more the tendency of the corresponding elastic post-buckling paths in Fig. 4 (middle graphs), also observed in graph (b). In comparison with section U1, a positive imperfection now leads to a much lower strength, which follows quite closely the highest Eurocode 3 buckling curves of both methods, namely that of clause 6.3.2.3.

(ii) For Case 3, graph (a) makes it possible to conclude that the buckling strengths for positive and negative imperfection are much closer than for Case 2 (as for section U1), but the χ_{LT} values now fall below the "perfect column" curve. Note that the paths in graph (c), although asymmetric, are not in perfect agreement with the elastic ones in Fig. 4 for this case. In particular, a lower strength for a negative imperfection (in agreement with the elastic post-buckling paths) is only obtained for the two higher slenderness values, since for the lower values, χ_{LT} is higher for negative imperfections — this may be attributed to the shift of the

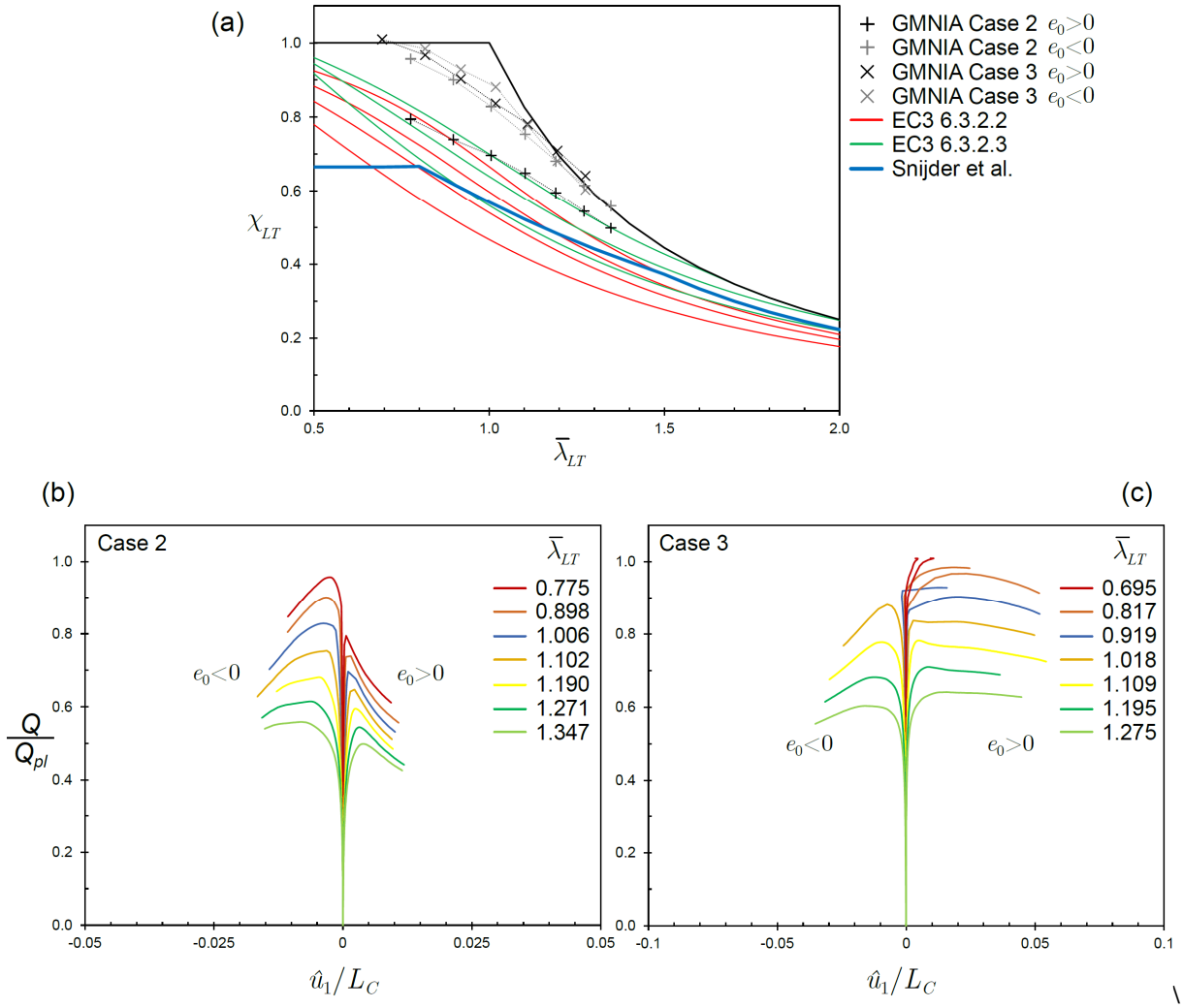

Figure 7: GMNIA results for Cases 2 and 3 and cross-section U2: (a) reduction factors and (b)-(c) normalized load-displacement paths.

shear center as plasticity spreads, as previously mentioned. In fact, note that for $\bar{\lambda}_{LT} \leq 0.919$ the paths with negative imperfection shift to positive displacement as a result of this effect — a load applied at the elastic shear center becomes eccentric (with positive eccentricity) and triggers positive $\hat{u}_1$ displacements.

In general terms, the results displayed in graphs (a) in Figs. 6 and 7 display a significant scatter, with a strong dependency on the cross-section geometry, the imperfection direction and the load/support conditions. Nevertheless, it is noted that, for a given imperfection/load/support, the resistance is much lower for cross-section U2, in agreement with the elastic post-buckling curves displayed in Fig. 4 (in general, the paths for section U2 fall below those of section U1). It can be therefore concluded that it is not economic to define a single buckling curve for design purposes. For the cases analyzed, the Eurocode 3 provisions they lead to very conservative strength estimates and the method proposed by Snijder et al. (2008), although developed for eccentric loads, also leads to conservative results, but not as conservative as those of Eurocode 3.

4. Conclusions

This paper provided a new insight into the elastic post-buckling behavior and strength of steel channel beams undergoing lateral-torsional (LT) buckling. Three cross-sections and three support/load conditions were analyzed using a geometrically exact beam finite element previously developed by the author, which can handle large displacements, including torsion-related warping, Wagner effects, plasticity, residual stresses and geometric imperfections.

From all the results obtained, the following main conclusions are highlighted:

(i) The elastic LT post-buckling behavior of channel beams is asymmetric and, in some cases, exhibit negative stiffness near the bifurcation load. The shape of the elastic post-buckling equilibrium path is strongly influenced by the direction of the geometric imperfection, the support/load conditions and the cross-section geometry.

(ii) Their strength of channel beams, obtained through GMNIAs (geometric and material non-linear analyses including geometric imperfections and residual stresses), is also significantly influenced by the direction of the geometric imperfection, the support/load conditions and the cross-section geometry. This leads to a large scatter of strength values.

(iii) The large scatter observed demonstrates that the definition of a single buckling curve is not economic. Nevertheless, for all cases considered, the Eurocode 3 provisions lead to safe results (although very conservative) and the method proposed by Snijder et al. (2008), although developed for eccentric loads (thus incorporating first-order torsion effects), obviously leads to conservative results, but not as conservative as those of Eurocode 3.

Future work will focus on the development of appropriate buckling curves for channel section beams.

References

Bathe, K.J. (2019). *ADINA System*, ADINA R&D Inc.

CEN (2005). *EN 1993-1-1:2005, Eurocode 3: Design of Steel Structures — Part 1-1: General Rules and Rules for Buildings*. Belgium, Brussels: CEN.

Frickel, J. (2002). "Bemessung von Trägern unter Biegung und Torsion nach Th. II. Ordnung." *Rubstahl-Bericht* (2) 1-4.

Gonçalves, R. (2012). "A geometrically exact approach to lateral-torsional buckling of thin-walled beams with deformable cross-section." *Computers and Structures*, 106-107 9-19.

Gonçalves, R. (2016). "A shell-like stress resultant approach for elastoplastic geometrically exact thin-walled beam finite elements." *Thin-Walled Structures*, 103 263-272.

Gonçalves, R., Camotim, D. (2017). "A system-based approach for the design of laterally unbraced multi-span steel columns and beams." *Engineering Structures*, 135 10-20.

Gonçalves, R. (2019). "An assessment of the lateral-torsional buckling and post-buckling behaviour of steel I-section beams using a geometrically exact beam finite element." *Thin-Walled Structures*, 143 106222.

Gonçalves, R. (2020). "An assessment of the Eurocode 3 provisions for lateral-torsional buckling of I-sections under uniaxial and biaxial bending." *Proceedings of the Annual Stability Conference, Structural Stability Research Council,* Atlanta, Georgia, 1-18.

Gruttmann, F., Sauer, R. Wagner, W. (2000). "Theory and numerics of three-dimensional beams with elastoplastic material behaviour." *Internatonal Journal for Numerical Methods in Engineering*, 48 (12) 1675-1702.

Handelman, G.H. (1951). "Shear center for thin-walled open sections beyond the elastic limit." *Journal of the Aeronautical Sciences*, 18 (11) 749-754.

Johnson, W., Mellor, P. (1957). "The centre of shear for a material having a non-linear stress-train curve." *Applied Scientific Research, Section A*, 6 (5-6) 467-477.

Kindmann, R., Frickel, J. (2002). "Tragfähigkeit von U-Profilen bei Biegung und Torsion." *Rubstahl-Bericht* (1) 1-2.

Kindmann, R., Wolf, C. (2004). “Ausgewählte Versuchsergebnisse und Erkenntnisse zum Tragverhalten von Stäben aus I- und U-Profilen.” *Stahlbau*, 73 (9) 683-692.

Kwon, Y., Hancock, G. (1993). “Post-buckling analysis of thin-walled channel sections undergoing local and distortional buckling.” *Computers and Structures*, 49 (3) 507-516.

Lindner, J., Glitsch, T. (2004). “Vereinfachter nachweis für I- und U-träger beansprucht durch doppelte Biegung und Torsion.” *Stahlbau*, 73 (9) 704-715.

Martins, A., Camotim, D., Gonçalves, R., Dinis, P. (2018). “On the mechanics of local-distortional interaction in thin-walled lipped channel beams.” *Thin-Walled Structures*, 128 108-125.

MATLAB (2010). Version 7.10.0 (R2010a), *The MathWorks Inc.*, Massachusetts.

Pi, Y., Trahair, N. (1992). “Prebuckling deflections and lateral buckling. II: Applications.” *Journal of Structural Engineering*, 118 (11) 2967-2985.

Reissner, E. (1972). “On one-dimensional finite-strain beam theory: The plane problem.” *Zeitschrift für angewandte Mathematik und Physik*, 23 (5) 795-804.

Reissner, E. (1973). “On one-dimensional large-displacement finite-strain beam theory.” *Studies in Applied Mathematics*, 52 87-95.

Simo, J. (1985). “A finite strain beam formulation. The three-dimensional dynamic problem. Part I.” *Computer Methods in Applied Mechanics and Engineering*, 49 (1) 55-70.

Simo, J., Vu-Quoc, L. (1991). “A geometrically-exact rod model incorporating shear and torsion-warping deformation.” *International Journal of Solids and Structures*, 27 (3) 371-393.

Snijder, H., Hoenderkamp, J., Bakker, M., Steenbergen, H., de Louw, C. (2008). “Design rules for lateral-torsional buckling of channel sections subject to web loading.” *Stahlbau*, 77 (4) 247-256.

Taras, A., Greiner, R. (2010). “New design curves for lateral-torsional buckling-proposal based on a consistent derivation.” *Journal of Constructional Steel Research*, 66 (5) 648-663.

Vlasov, V. (1958). *Tonkostenye Sterjni*. Fizmatgiz, Moscow, Russia.

Wagner, H. (1929). “Verdrehung und Knickung von offenen Profilen.” *Fünfundzwanzig Jahre Technische Hochschule Danzig*, Danzig (Gdańsk), Poland, 329-344.

Ye, J., Meza, F., Hajirasouliha, I., Becque, J., Shepherd P., Pilakoutas, K. (2019). “Experimental investigation of cross-sectional bending capacity of cold-formed steel channels subject to local-distortional buckling interaction.” *Journal of Structural Engineering*, 145 (7) 04019064.

Trahair, N. (1993). *Flexural-Torsional Buckling of Structures*. Taylor & Francis.